NANO LETTERS

Letter

pubs.acs.org/NanoLett

Topographically-Designed Triboelectric Nanogenerator via Block Copolymer Self-Assembly

Chang Kyu Jeong,[†,§] Kwang Min Baek,[†,§] Simiao Niu,[‡] Tae Won Nam,[†] Yoon Hyung Hur,[†] Dae Yong Park,[†] Geon-Tae Hwang,[†] Myunghwan Byun,[†] Zhong Lin Wang,[‡] Yeon Sik Jung,*[,†] and Keon Jae Lee*[,†]

[†]Department of Materials Science and Engineering, Korea Advanced Institute of Science and Technology (KAIST), 291 Daehak-ro, Yuseong-gu, Daejeon, 305-701, Republic of Korea

[‡]School of Materials Science and Engineering, Georgia Institute of Technology, Atlanta, Georgia 30332-0245, United States

Supporting Information

ABSTRACT: Herein, we report a facile and robust route to nanoscale tunable triboelectric energy harvesters realized by the formation of highly functional and controllable nanostructures via block copolymer (BCP) self-assembly. Our strategy is based on the incorporation of various silica nanostructures derived from the self-assembly of BCPs to enhance the characteristics of triboelectric nanogenerators (TENGs) by modulating the contact-surface area and the frictional force. Our simulation data also confirm that the nanoarchitectured morphologies are effective for triboelectric generation.

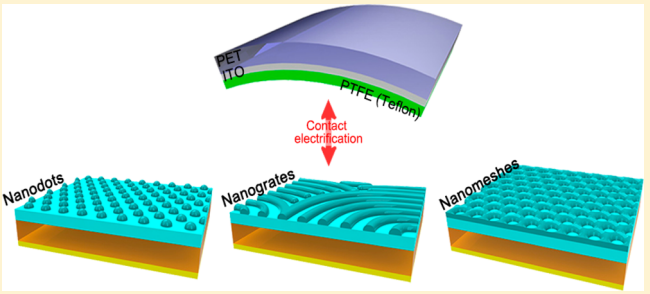

KEYWORDS: *Block copolymer, self-assembly, triboelectrification, triboelectric nanogenerator, energy harvesting*

The rapid and tremendous expansion of wireless, portable, and wearable electronics has significantly underscored the common need for effective and affordable renewable energy sources, which are becoming increasingly important to their operation.[1,2] The conversion of mechanical energy from an ambient environment to electrical energy, based on electrostatic interaction,[3,4] piezoelectricity,[5−12] and electromagnetic induction,[13,14] has been regarded as one of the most promising of the emerging energy harvesting technologies currently under development. Recently, a new concept of innovative energy harvester was developed which utilizes the well-known triboelectrification phenomenon, called a triboelectric nanogenerator (TENG).[15] The triboelectric effect can be defined as a charge transfer process enabled by contact electrification between two different materials that exhibit distinct tribopolarity.[16] Irregular mechanical energy sources, such as ambient infrastructural vibration, human walking, and transportation movement, are the highly common and available energy sources in our surroundings, which can be potential sources for triboelectric energy harvesting. Therefore, this triboelectric approach is well-suited to harvesting power from ambient energy sources in an extremely simple, robust, and scalable manner.

Since Fan et al. first reported the concept of TENG in early 2012,[17] there have been rapid advances in the field which have extended its potential applications, from powering the electronics of micro/nanosystems[18−20] to establishing large-scale electricity generation[21,22] corresponding to a traditional electromagnetic generator. To achieve high-performance TENGs, three main factors have to be considered: material selection, device structure, and contact surface morphology.[15] Until now, the majority of intensive studies aimed at enhancing the performances of TENGs have focused primarily on innovative materials[23−27] and device structures.[19,25,28−32] In contrast, less attention has been paid to the surface morphology, although the morphological features of the contact area can exert a strong influence on contact-induced charges and frictional electrification. Micrometer-scale patterning based on conventional photolithography has been applied to the fabrication of TENGs to overcome the limited triboelectric properties of natural flat surface. However, relatively bulky surface structures at the micrometer scale can give rise to an undesirable excessive friction force, which may degrade the energy conversion efficiency of the TENGs.[15] Although various approaches using surface morphologies at the nanometer scale (e.g., anodic aluminum oxide (AAO),[19] surface-linked nanoparticles (NPs),[33] polymer dry-etching,[34] etc.[35−39]) have been applied for enhancing triboelectrification, most of them have critical limitations such as limited controllability, restricted material selection, irregular topology, fixed morphologies, and weak mechanical properties. Therefore, an in-depth study on the effect of nanoscale surface topographies and morphologies which can significantly

Received: September 4, 2014
Revised: October 29, 2014

dx.doi.org/10.1021/nl503402c | *Nano Lett.* XXXX, XXX, XXX−XXX

influence contact characteristics and device performances is still highly needed.[15]

Block copolymer (BCP) self-assembly, which is induced by the microscopic phase separation of covalently linked polymer blocks, is currently of great interest as an alternative strategy for achieving densely arranged nanoscale patterns including dots, lines, holes, and rings.[40−44] In comparison with conventional photolithography, BCP self-assembly has distinct advantages—especially higher resolution and cost-effectiveness.[45] The ultimate resolution of BCP self-assembly has been reported to be below 5 nm,[46−50] which is far below the resolution limit of general photolithography. Moreover, the formation of high-resolution patterns is possible over a large-area wafer-scale (8 in.) in a fast and cost-effective manner.[48,51] Inspired by the above-mentioned advantages, BCP self-assembly has been utilized to demonstrate various practical devices such as sensors,[52,53] electronics,[54−57] energy devices,[58] and patterned magnetic recording media.[59] However, despite its outstanding potential, BCP technology has not been tried as a solution to improve the contact-charging surfaces in triboelectric applications.

Most of the recent studies of triboelectric energy harvesting technologies have focused on only the way to improvement of output current. The fundamental innovation should be dealt for the investigation of versatile surface morphology related to performance of TENGs on the basis of new approaches. Using the BCP technology, we designed the study which can bring together a very broad range from academic to practical disciplines for breakthrough in TENG technologies. Here in this work, we demonstrate a new concept of TENGs design enabled by BCP self-assembly, as a bottom-up approach to control the morphologies of contact surfaces at the nanometer scale and modify frictional properties, thus significantly enhancing device performance. Among numerous self-assembling BCP systems, we chose polystyrene-*block*-polydimethylsiloxane (PS-*b*-PDMS) which can be readily converted into silica nanostructures by simple oxidation. PS-*b*-PDMS can be self-assembled into spatially defined PDMS microdomains in PS matrix including spheres, cylinders, and perforated lamellae, which can form silica nanodots, nanogrates, and nanomeshes after selectively removing the PS and oxidizing the PDMS. The nanostructured silica film was combined with Teflon as a counterpart surface to enable effective contact electrification. The overall area of the silica nanopatterned surface can be increased by up to ∼70%, strongly depending on the geometry of the self-assembled BCP nanodomains. The resulting short-circuit current and the corresponding output power were observed to be ∼2.5 times and ∼6.3 times higher than those of a nonpatterned TENG. The output power generated by the BCP-assisted TENG device was high enough to drive commercial electronic components such as LED bulbs and capacitors without external power sources. The TENGs containing self-assembled BCP nanostructures were further characterized using simulations and frictional tests. We believe that this work can provide a new strategy to develop highly effective triboelectric energy harvesting devices in a facile and robust manner, accelerating the realization of TENG-based self-powered electronic/sensor systems.

The overall fabrication procedures for nanopatterned TENGs enabled by BCP self-assembly (BCP-TENGs) are schematically illustrated in Figure 1a. Polyimide (PI) flexible substrate (Kapton) was selected as a starting material for the bottom parts of the BCP-TENGs owing to its excellent

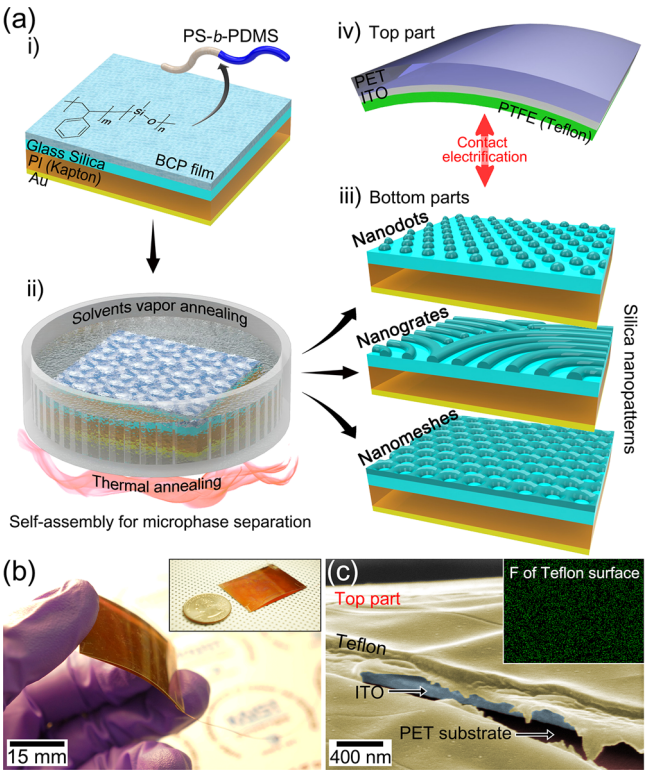

Figure 1. (a) Flowchart of the fabrication scheme for the BCP-TENGs. (i) Spin-casting of PS-*b*-PDMS BCP solutions on the Au/Kapton PI/glass silica substrate. (ii) Thermal and solvent vapor annealing to induce microphase separation of BCP films. (iii) Various silica nanopatterns achieved by the tunable BCP self-assembly for effective triboelectricity generation. These are the bottom parts of diverse BCP-TENGs. (iv) Merging the arch-shaped top part (Teflon PTFE/ITO/PET) with the bottom part for contact electrification. (b) The photographs of as-fabricated BCP-TENG device. (c) Cross-sectional colorized SEM image of the top part of the BCP-TENGs to show the reliably constructed solution-processed Teflon film. Inset: An EDS elemental mapping result of F in the Teflon film.

chemical resistance, decent dielectric constant, lightweight, and easy handling. Cr/Au and glass silica were deposited on both sides of the PI substrate by electron-beam evaporation, as a bottom electrode and a positively charged triboelectric surface, respectively. For efficient triboelectrification, glass silica was chosen because it occupies the rank of most positively charged material in the triboelectric series, even above Nylon, fur, or normal silicon oxide.[16] Solutions of PS-*b*-PDMS in a mixture of toluene, heptane, and propylene glycol monomethyl ether acetate were spin-coated onto glass silica substrates modified with hydroxylated PS brush (Figure 1a,i). The BCP thin film on top of the brush layer covering the glass silica layer was then solvent- or solvothermally annealed in a sealed jar under saturated toluene vapor to induce the self-assembly of the PS-*b*-PDMS (Figure 1a,ii).

Among various kinds of functional BCPs, we chose PS-*b*-PDMS for two principal reasons, as follows. First, PS-*b*-PDMS more readily accomplishes an organic to inorganic structural transformation compared to other BCPs. Although many kinds of BCPs are widely used as nanopatterning tools for universal materials, most of them require additional subsequent pattern-transfer steps such as lift-off or etch-back processes.[42,45,49] In contrast, the self-assembly of PS-*b*-PDMS can readily construct diverse silica nanostructures through a single-step CF_4/O_2

dx.doi.org/10.1021/nl503402c | *Nano Lett.* XXXX, XXX, XXX−XXX

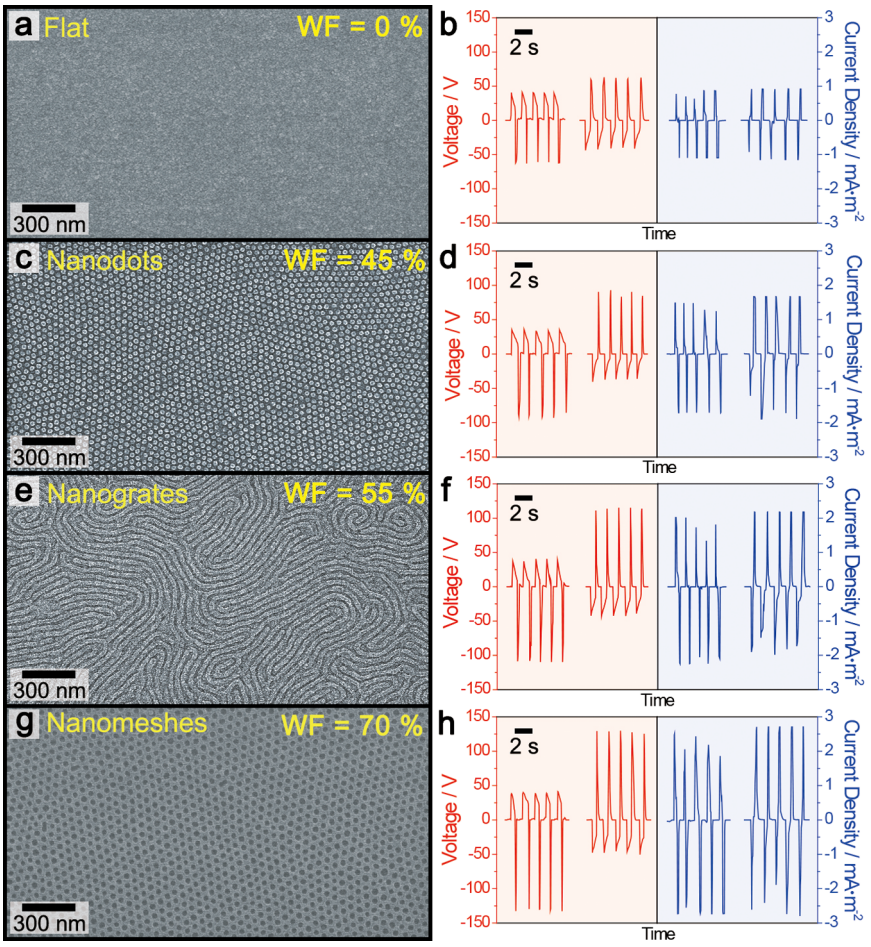

Figure 2. SEM images of bottom parts' surface morphologies and the forward/reverse signals of generated electricity of (a,b) flat TENG, (c,d) nanodots BCP-TENG, (e,f) nanogrates BCP-TENG, and (g,h) nanomeshes BCP-TENG, respectively.

plasma treatment.[60] It should be noted that the nanostructured material should be the same as the underlying triboelectric surface (amorphous silica in our case) to explore the effect of nanoscale topography on TENGs. Second, PS-*b*-PDMS has a lot higher Flory–Huggins interaction parameter (χ) than other BCPs; χ describes the incompatibility between each polymer block, which is a crucial factor for microphase separation in BCP systems.[60] Accordingly, PS-*b*-PDMS can guarantee long-range ordered nanostructures down to sub-10 nm scale over wafer-scale substrates, as confirmed by grazing-incidence small-angle X-ray scattering (GISAXS) in our previous reports.[48]

In the present work, the BCP thin film was spontaneously rearranged and transformed into various nanoscale morphologies such as spheres, lateral cylinders, and hexagonally perforated lamellae (HPL). The types of morphology are mainly governed by the molecular weight (MW) and the volume fraction (f) of each polymer block. Subsidiary control over domain size and arrangement can also be achieved by varying the solvent and the duration time of solvent-vapor annealing. The use of solvents with different affinities for PS and PDMS blocks, respectively, can be beneficial for the control of self-assembled nanopatterns. Subsequently, O_2 plasma treatment was conducted to remove the PS blocks and convert the PDMS domains into silica nanopatterns, which occurs as a result of the plasma oxidation of the Si components in the PDMS blocks. Silica nanostructures were generated, as depicted in Figure 1a,iii: spheres (nanodots), fingerprint-like cylinders (nanogrates), and gyroid-based HPL (nanomeshes) formed by three kinds of PS-*b*-PDMS BCPs with different MWs of 47.1–9, 31–14.5, and 22–14 kg·mol^{-1}, which correspond to PDMS volume fractions (f_{PDMS}) of 16.0%, 31.9%, and 38.9%, respectively.

To prepare the counterpart triboelectric surface for contact-induced negative charges, a PTFE-based Teflon thin film was cast on an indium tin oxide (ITO)-coated polyethylene terephthalate (PET) substrate (Figure 1a,iv); PTFE-based Teflon ranks as the most negative material in the triboelectric series. The selection of two materials from the triboelectric series which are significantly separated from each other is highly important for TENGs, to induce a large charge transfer between the materials. The Teflon-coated ITO/PET substrate was faced to the nanopatterned silica layer on the Kapton/Au substrate, then the two substrates were sealed along the long axis by PET tape at the edges. This formed an arch-shaped TENG, since the top part was slightly longer than the bottom part. The details of the fabrication protocols are discussed in the Supporting Information.

Figure 1b shows a photograph of an as-fabricated BCP-TENG, which is light and flexible due to the use of plastic substrates. The central gap distance between the top and bottom parts of our TENGs was designed to be about 2 mm, which had been reported as the optimized distance for arch-shaped TENGs in previously studies.[25,61] Wang et al. reported that output potential and power were gradually increased by

dx.doi.org/10.1021/nl503402c | *Nano Lett.* XXXX, XXX, XXX–XXX

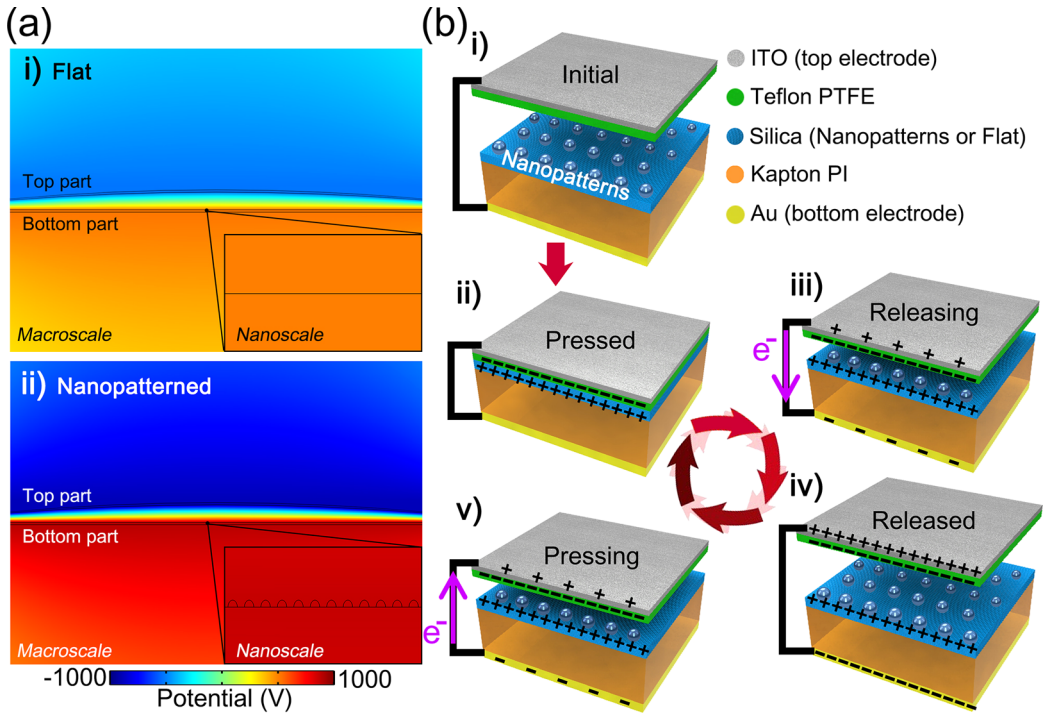

Figure 3. (a) Color-coded simulation results showing triboelectric potential differences of (i) flat and (ii) nanopattern silica surfaces with the Teflon PTFE top part. (b) Schematics that present the working mechanism of the TENGs. (i) Initial state without pressing force. (ii) Contact status by an applied force, with the triboeletrification inducing positive charges on the bottom silica surface and negative charges on the top Teflon film. (iii) Removal of the applied force causing the separation of triboelectric-charged layers. Produced potential difference drives the flow of electrons through the external load. (iv) The top part completely returning back to the initial position. The triboelectric charges are completely screened by induced charges to balance the potential difference. (v) The applied force brings the top and bottom parts to contact again, which generates electron flow in the reverse direction.

increasing the gap distance before reaching the saturation point.[25] Mechanical pressure on the curved top part leads to close contact with the nanopatterned bottom part, and then after the pressing force disappears, the two parts are instantaneously separated again because of the stored elastic energy and resilience of the curved top part. The air-gap of the arch-shaped TENG also plays a role in increasing capacitance, i.e., an increase in the strength of dipole moments generated by contact electrification.[24,25] Figure 1c presents a cross-sectional tilted scanning electron microscopy (SEM) image of the top part, composed of Teflon/ITO/PET layers. The Teflon thin film (200 nm in thickness) was formed on top of the ITO/PET substrate through spin- or dip-casting methods, as confirmed in previous studies.[62] The fluorine component of the PTFE-based Teflon thin film was well-characterized by energy dispersive X-ray spectroscopy (EDS) elemental mapping images, as shown in the inset of Figure 1c and Figure S1.

We characterized the surface morphologies of the evaporation-deposited silica film and nanostructured silica surfaces derived from BCP to compare their nanoscale morphologies. As clearly shown in the SEM images in Figure 2a, the nonpatterned silica surface of the bottom part was flat (i.e., flat TENG). In contrast, the BCP self-assembly produced three different types of nanopatterns including spherical nanodots, fingerprint-like nanogrates, and perforated lamellar nanomeshes over the whole area of the bottom part as shown in Figure 2c,e,g and Figure S3. As exhibited in these SEM images, the widths of the silica nanopatterns prepared from PS-*b*-PDMS BCPs were controlled to be about 20 nm. The cross-sectional images of these nanoarchitectures exhibit nonangulated humpy (regularly arranged smooth) structures with a height of ~15 nm (Figures S4–S6). According to the geometrical consideration and fill factor calculation, the area widening ratio of each nanostructure with respect to the flat surface can be calculated; this ratio is defined as a widening factor (WF = [difference of area between nanopatterned and flat surface/area of flat surface] × 100%).[54] The resulting WFs of each morphology (i.e., nanodots, nanogrates, and nanomeshes) were calculated to be approximately 45%, 55%, and 70%, respectively. Interestingly, it was experimentally proven that varying the self-assembled BCP nanodomain structures with different WFs played a critical role in increasing the contact charging area and the friction effect in the triboelectric power generation mechanism.

As presented in Figure 2b, the arch-shaped flat TENG generated voltages and current densities of up to ~63 V and ~1.1 mA·m^{-2}, respectively, when the vertically compressive force of 50 N was applied. In clear contrast, Figure 2d,f,h manifests that the open-circuit output voltage and short-circuit current density signals of the BCP-TENGs patterned at nanoscale with nanodots, nanogrates, and nanomeshes were measured to have increased from ~95 V and ~1.8 mA·m^{-2}, to ~110 V and ~2.3 mA·m^{-2}, and to ~130 V and ~2.8 mA·m^{-2}, respectively. Such remarkable improvement in the output power of the nanopatterned BCP-TENGs with increasing WFs can be rationalized as follows; the nanopatterned surfaces with more sophisticated morphologies can be expected to give rise to larger triboelectric contact area and stronger friction, which can result in more surface charges compared to nonpatterned surfaces. Hence, the silica surfaces with various nanostructures

dx.doi.org/10.1021/nl503402c | *Nano Lett.* XXXX, XXX, XXX–XXX

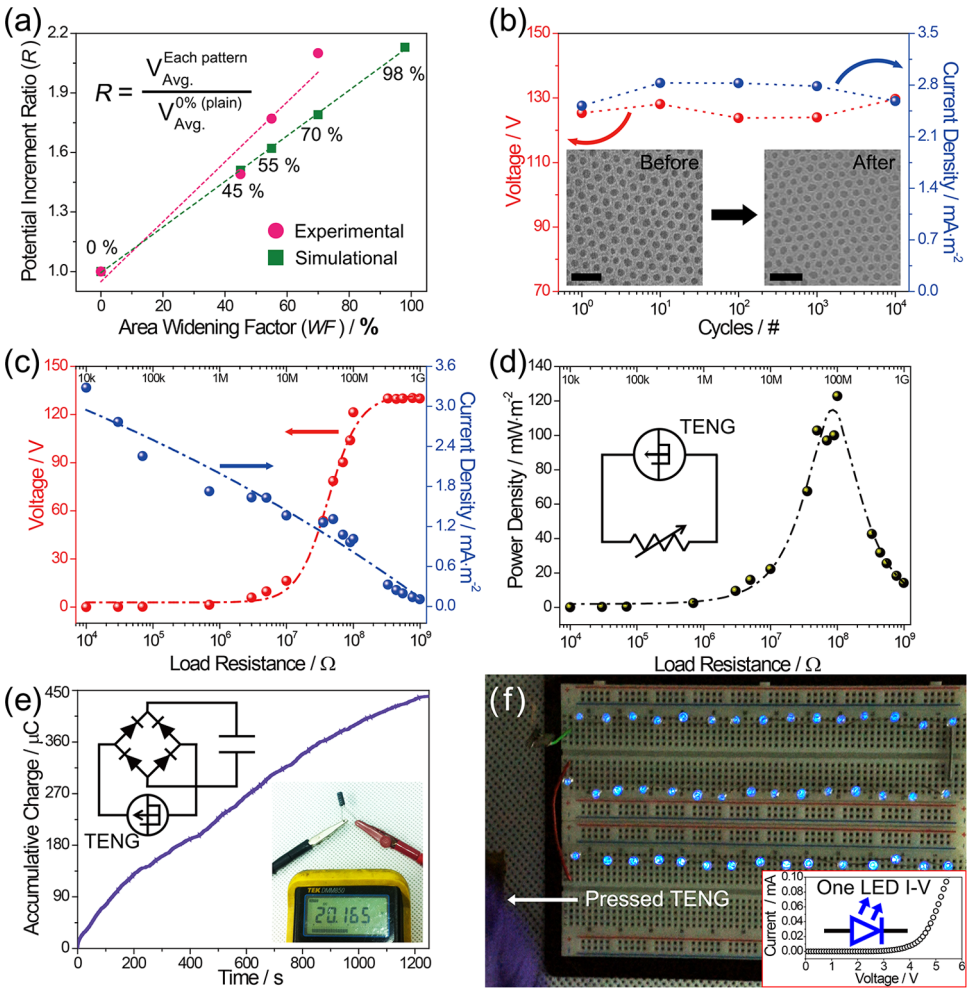

Figure 4. (a) Degree of increased electric potential according to the area WF (related to nanopatterning) in the experimental and simulation data. In the experiments, the nanomeshes BCP-TENG (WF = 70%) show the highest electrical output. (b) The durable performance of the nanomeshes BCP-TENG at each cyclic point. The insets show that the nanoscale surface morphology is not changed after 10 000 cycles with ~70 kgf. (c) Output voltage and current density of the BCP-TENG depending on the external load resistance. (d) Instantaneous power density according to the function of variable resistance, which is calculated by the product of current density squared and load resistance. (e) Charging a capacitor by the output electricity generated by the nanomesh BCP-TENG with a rectifying circuit (left inset). The charged voltage after 20 min is about 20 V (right inset). (f) 45 blue LEDs in series are directly driven by the generated electricity from the nanomesh BCP-TENG without any external energy sources. The inset shows the turn-on voltage of one blue LED (~3 V) in the current–voltage curve.

produced up to ~2.5 times improvement in current generation (and ~6.3 times enhancement in output power) compared to the flat surface. It should be noted that the output voltage signals of pressed states were not dependent on the surface patterns, whereas those of released states apparently changed depending on the different types of surfaces. This is presumably because the charge screening mechanism for an intimately contacted state (fully pressed state) would not be specifically related to the surface morphologies in the device structure of our TENG. The detailed mechanism of our TENG is explained in a later part.

To further confirm the effects of BCP nanopatterns on triboelectric potential, we also conducted analytical simulations using a finite element method (FEM) with COMSOL software (Figure 3a). In clear comparison with the flat TENG (Figure 3a,i), the triboelectric potential of the BCP-TENG proportionally increases as the contact area becomes larger compared to that of a flat TENG, since the BCP nanopatterned surface has a larger contact charging area, which causes higher charge density (σ) on the electrificated surfaces (Figure 3a,ii). As a result, the transferred charges (Q) between electrodes can increase as the triboelectric charge density increases, as expressed in the following eq 1

$$Q = \frac{\sigma d' \varepsilon_{r1} \varepsilon_{r2}}{t_1 \varepsilon_{r2} + d' \varepsilon_{r1} \varepsilon_{r2} + t_2 \varepsilon_{r1}} \quad (1)$$

where d' is the gap distance between two surfaces, ε_{r1} and ε_{r2} are the relative permittivity of two dielectric materials, and t_1 and t_2 are the thickness of the two triboelectric layers, respectively.[34]

Triboelectric potential (V) can also be enhanced by the surface topography because it is related to the value of σ and Q. The maximum V of the model for the dielectric-to-dielectric contact mode TENG is described as

$$V = -\frac{Q}{S\varepsilon_0}\left(\frac{t_1}{\varepsilon_{r1}} + \frac{t_2}{\varepsilon_{r2}} + d'\right) + \frac{\sigma d'}{\varepsilon_0} \quad (2)$$

where S is the area of the electrode and ε_0 is vacuum permittivity.[63]

dx.doi.org/10.1021/nl503402c | Nano Lett. XXXX, XXX, XXX–XXX

Consequently, the larger contact surface area with nanostructures enables the superior production of higher transferred charges and triboelectric potential differences for triboelectric energy harvesting. Although previously reported high aspect-ratio nanowires (NWs) for TENGs can have wider contact area compared to our BCP nanopatterns, they are mechanically fragile (inorganic NWs) or deformable (polymeric NWs) due to their inherent mechanical characteristics (Figure S7a,b).[34,35] Even if mechanically strong high aspect-ratio nanostructures are used for triboelectrification (e.g., nanosheets and AAO templates), the real contact area cannot be large because the counterpart contact materials cannot penetrate deeply into the whole nanostructures, because of their limited solid ductility (Figure S7c).[64] Therefore, the triboelectrification efficiency of low aspect-ratio nanostructures, such as our BCP nanopatterns or NPs, can be similar or even superior to that of high-aspect ratio nanostructures.[18,33]

The working principle of the TENG can be explained by the coupling effect between contact triboelectrification and electrostatic induction,[15] as schematically illustrated in Figure 3b. In the original state before initial contact (Figure 3b,i), there is no charge transfer. This does not occur until the two parts of the BCP-TENG are brought into contact by external force (i.e., mechanical pressure causing the arch-type top part to be flattened, thus leading to close contact with the bottom part). When the Teflon PTFE surface is in close contact with the nanopatterned silica surface, triboelectric charges are produced at the contact surfaces—negative charges on the top surface and positive charges on the bottom surface, as shown in Figure 3b,ii. Anions are donated from the material on the more positive side in the triboelectric series to the other, more negative side. When these two surfaces are subsequently separated, the negative and positive triboelectric charges are not completely removed but still remain on the surfaces of the Teflon PTFE and nanopatterned silica for a prolonged period of time, thus inducing the opposite charges on the surfaces of the ITO and the Kapton PI (Figure 3b,iii). Consequently, the electric potential difference between the two parts results in electron flow through external loads to satisfy the entire electrical balance (Figure 3b,iv). As described in eq 1, the silica and Teflon PTFE layers in our TENGs are expected to be highly beneficial for inducing charge transfer because they can be easily fabricated as thin films by the methods described above. Changing the gap distance between two surfaces leads to different charge distribution in the TENGs, thus finally establishing a new equilibrium at the fully released state (Figure 3b,iii and iv). When the external pressure is applied to the top part again, the dipole moments in the gap starts decreasing as the two surfaces get closer to each other (Figure 3b,v). Changing the electric potential difference causes electron flow from the bottom electrode to the top electrode, removing the accumulated charges. Note that, on mechanical pressing, a reciprocal screening between the triboelectric charges on the two contact surfaces can be achieved, regardless of the amount of triboelectric charge density related to the surface morphology. The mechanism of TENG is similar to the similar to the principles of dielectric elastomer actuator.[65]

To investigate the more detailed process of contact electrification in our TENG devices, we performed X-ray photoelectron spectroscopy (XPS) and electric force microscopy (EFM). The XPS analysis results revealed that, after reciprocating contact cycles (~10 000), the Si binding energy is significantly decreased, indicating the loss of oxygen in the silica surface (Figure S8).[66] In addition, the oxygen fraction in the counterpart Teflon film was increased, as shown in Figure S9. These results suggest that the contact electrification was induced by the transfer of surface ions ($-O^-$ and OH^-) from silica to Teflon layer through mechanical contact, because triboelectricity between insulators can be explained by ion transfer rather than electron transfer, as previously reported.[16,67−69] The transferred ionic charges can persistently act as the triboelectric potential because the tribo-charges on insulators can be retained and not be leaked out for an extended period time.[15,34,70] The removal of negative ions from the silica surface can cause uncompensated silicon/silica cations. Furthermore, some sequential electron movements from transferred oxygen-related ions to fluorine components in Teflon may be expected due to the highest electronegativity of fluorine. The EFM data, showing the changed relative potential of silica surface in a phase map, also support this mechanism based on the transfer of oxygen-related ions (Figure S10).

In order to further confirm the effect of area widening on the increment of potential, we carefully performed COMSOL simulations, as plotted in Figure 4a. The simulation results showed a potential increase with an increase in the contact area, which is consistent with our experimental results. However, intriguingly, the dependence of potential on the contact area was higher than the experimental result. For example, for the WF of over 90%, a doubled potential difference was achieved in the case of the simulation result, while the same potential difference was obtained at a lower WF (~70%; nanomesh) in the experiment. This inconsistency is presumably because of the higher frictional force on the nanomesh surface compared to the flat surface in the real experiments, as presented in the measured frictional coefficients with Teflon thin film for each silica nanostructure (Figure S11). Frictional force is not simply related to contact surface area, whereas it is dependent on surface morphologies and properties. According to the previous reports, frictional events can occur in contact-mode TENGs because the mechanical compressive force between two layers results in relative sliding events at micro/nanoscale topographies, despite no macroscopic lateral sliding.[15,17,71] Due to the increased frictional events, the generation of triboelectric charges can also be more enhanced during the contact and separation process.[15,17] Therefore, our experimental observation is closely consistent with the fact that the bumpier nanostructure can lead to the higher frictional force.

A nanomesh-embedded BCP-TENG was selected for detailed characterizations since it had the highest performance among the different BCP-TENGs. The mechanical durability of the BCP-TENG with nanomesh structures was confirmed by repeated impacts of 70 kgf as shown in Figure 4b. During cyclic impacts, neither the output voltage nor the current density were significantly degraded, and in the meantime the nanomesh-structured surface was not morphologically changed as shown in the insets of Figure 4b. The Teflon PTFE surface of top part was also not damaged after the durability test (Figure S10a and Figure S12). Wear and abrasion, which can happen when two solid bodies are rubbed, are significant in sliding/rotating-type triboelectric energy harvesters.[15,21] In contrast, the simple contact-type configuration such as our arch-shaped TENG is beneficial for mechanical wear resistance compared to sliding/rotating-type TENGs. Moreover, this good wear resistance was attributed to the specific plasma treatment methods, as previously reported (see Supporting Information).[21,72,73] The Teflon PTFE counterpart surface was also not mechanically

dx.doi.org/10.1021/nl503402c | Nano Lett. XXXX, XXX, XXX−XXX

imprinted or stamped (e.g., nanoimprinting) due to the high viscosity in solid state and excellent creep resistance, as well as the low aspect ratio of BCP nanopatterns.[74,75] The plots in Figure 4c show a gradual decrease in the output current density and an increase in the voltage across the resistors with increasing resistance. Markedly, the output voltage was saturated when the external load approached infinite resistance. The instantaneous output power density showed a maximum value of 122.8 mW·m^{-2} at the resistance of ∼100 MΩ (Figure 4d). In accordance with the above results, the BCP-TENG device structure provided the energy conversion efficiency of ∼18% at the device level, as calculated in previous reports (see the Supporting Information).[25]

To confirm the feasibility of the BCP-TENG for energy storage, a 22 μF capacitor was connected to the BCP-TENG with nanomesh-structures using a full-wave bridge rectifying circuit. The BCP-TENG under mechanical pressure at 3 Hz for about 20 min successfully charged the capacitor. Notably, the accumulated charge increased with time as shown in Figure 4e, suggesting the BCP-TENG had excellent stability. The charging rate was measured to be about 1 V·min^{-1}, allowing 20 min to store 20 V as shown in the inset of Figure 4e. The electric power produced by the BCP-TENG with nanomesh structures was used directly for turning on commercial light-emitting diode (LED) bulbs. During hand tapping the nanomeshes-type BCP-TENG, 45 blue LEDs were driven by the produced output voltage without the need for external energy storage devices (Figure 4f). By contrast, the BCP-TENG with nanodots was successful in turning on only about 30 LEDs. Considering the turn-on voltage of the LED bulb (inset of Figure 4f), these results confirm that the output voltage of the BCP-TENGs is strongly dependent on the morphologies (and consequently the WF) of the BCPs. The LED lights driven by the BCP-TENGs at various tapping frequencies are presented in Video S1 in the Supporting Information.

To summarize, we have developed nanoarchitectural triboelectric energy harvesters based on highly tunable nanoscale surface morphologies enabled by a facile and robust nanopatterning technique, BCP self-assembly. Various silica nanostructures including nanodots, nanogrates, and nanomeshes have been achieved by the controlled self-assembly of PS-*b*-PDMS thin film. Morphological variation in the self-assembled BCP nanopatterns provided simple control over the levels of contact area and friction that are critical for efficient triboelectrification. The nanoscale-tunable BCP-TENGs were achieved by applying the rational design of an arch-shaped structure with a PTFE-based Teflon thin film as a counterpart triboelectric surface. The nanostructured BCP-TENGs showed a pronounced improvement in output performance with voltage and current density of up to ∼130 V and ∼2.8 mA·m^{-2}, respectively, and the estimated energy conversion efficiency of ∼18% at device level. In particular, the TENG device embedded with a nanomesh-type BCP nanostructure achieved ∼2.5 times increase in current density, causing an almost 6.3 times enhancement in power generation compared to the nonpatterned flat TENG. The effects of the BCP nanopatterning on the triboelectric energy harvesting were systematically investigated by the calculation of area widening factors, measurement of friction coefficient, and analysis of numerical simulations. To shed light on the potential use of the BCP-TENG as a self-powered energy source, it was tested by building up charges in capacitors and directly operating multiple LED bulbs. Accordingly, it is highly expected that this versatile and practical BCP self-assembly process will open a more effective way to enhance the performances of triboelectric energy harvesting systems and broaden the application of triboelectrification phenomena, based on its facile convergence with established TENG-technologies such as various device structures,[28−31] different triboelectric modes,[76−78] sensor techniques,[33,35,37] and multiscale integrations.[19,64]

■ ASSOCIATED CONTENT

Ⓢ Supporting Information

All detailed experimental steps and related data/schematics. This material is available free of charge via the Internet at http://pubs.acs.org.

■ AUTHOR INFORMATION

Corresponding Authors

*E-mail: ysjung@kaist.ac.kr (Y.S.J.).
*E-mail: keonlee@kaist.ac.kr (K.J.L.).

Author Contributions

§C.K.J. and K.M.B. contributed equally to this work.

Notes

The authors declare no competing financial interest.

■ ACKNOWLEDGMENTS

This work was supported by the Basic Science Research Program (grant code: NRF-2012R1A2A1A03010415 and NRF-2013R1A1A2061440), Center for Integrated Smart Sensors as Global Frontier Project (CISS-2012M3A6A6054193 and CISS-2011-0031848) funded by the Korea government (MSIP) through the National Research Foundation of Korea (NRF).

■ REFERENCES

(1) Aricò, A. S.; Bruce, P.; Scrosati, B.; Tarascon, J.-M.; van Schalkwijk, W. *Nat. Mater.* **2005**, *4*, 366−377.
(2) Wang, Z. L. *Adv. Mater.* **2012**, *24*, 280−285.
(3) Peirine, R.; Kornbluh, R.; Eckerle, J.; Jeuck, P.; Oh, S.; Pei, Q.; Stanford, S. *Proc. SPIE* **2001**, *4329*, 148−156.
(4) Mitcheson, P. D.; Green, T. C.; Yeatman, E. M.; Holmes, A. S. *J. Microelectromech. Syst.* **2004**, *13*, 429−440.
(5) Wang, Z. L.; Wu, W. *Angew. Chem., Int. Ed.* **2012**, *51*, 11700−11721.
(6) Jeong, C. K.; Kim, I.; Park, K.; Oh, M. H.; Paik, H.; Hwang, G. T.; No, K.; Nam, Y. S.; Lee, K. J. *ACS Nano* **2013**, *7*, 11016−11025.
(7) Hwang, G.-T.; Park, H.; Lee, J. H.; Oh, S.; Park, K. I.; Byun, M.; Ahn, G.; Jeong, C. K.; No, K.; Kwon, H.; Lee, S. G.; Joung, B.; Lee, K. J. *Adv. Mater.* **2014**, *26*, 4880−4887.
(8) Persano, L.; Dagdeviren, C.; Su, Y.; Zhang, Y.; Girardo, S.; Pisignano, D.; Huang, Y.; Rogers, J. A. *Nat. Commun.* **2013**, *4*, 1633 DOI: ; 10.1038/ncomms2639.
(9) Mao, Y.; Zhao, P.; McConohy, G.; Yang, H.; Tong, Y.; Wang, X. *Adv. Energy Mater.* **2014**, *4*, 1301624.
(10) Jeong, C. K.; Park, K.-I.; Ryu, J.; Hwang, G. T.; Lee, K. J. *Adv. Funct. Mater.* **2014**, *24*, 2620−2629.
(11) Park, K.-I.; Son, J. H.; Hwang, G.-T.; Jeong, C. K.; Ryu, J.; Koo, M.; Choi, I.; Lee, S. H.; Byun, M.; Wang, Z. L.; Lee, K. J. *Adv. Mater.* **2014**, *26*, 2514−2520.
(12) Jeong, C. K.; Park, K.-I.; Son, J. H.; Hwang, G.-T.; Lee, S. H.; Park, D. Y.; Lee, H. E.; Lee, H. K.; Byun, M.; Lee, K. J. *Energy Environ. Sci.* **2014**, DOI: 10.1039/C4EE02435D.
(13) Beeby, S. P.; Torah, R. N.; Tudor, M. J.; Glynne-Jones, P.; O'Donnel, T.; Saha, C. R.; Roy, S. *J. Micromech. Microeng.* **2007**, *17*, 1257−1265.
(14) Galchev, T. V.; McCullagh, J.; Peterson, R. L.; Najafi, K. *J. Micromech. Microeng* **2011**, *21*, 104005.

(15) Wang, Z. L. *ACS Nano* **2013**, *7*, 9533−9557.
(16) McCarty, L. S.; Whitesides, G. M. *Angew. Chem., Int. Ed.* **2008**, *47*, 2188−2207.
(17) Fan, F. R.; Tian, Z. Q.; Lin Wang, Z. *Nano Energy* **2012**, *1*, 328−334.
(18) Zhu, G.; Lin, Z. H.; Jing, Q.; Bai, P.; Pan, C.; Yang, Y.; Zhou, Y.; Wang, Z. L. *Nano Lett.* **2013**, *13*, 847−853.
(19) Bai, P.; Zhu, G.; Lin, Z. H.; Jing, Q.; Chen, J.; Zhang, G.; Ma, J.; Wang, Z. L. *ACS Nano* **2013**, *7*, 3713−3719.
(20) Meng, B.; Tang, W.; Too, Z.; Zhang, X.; Han, M.; Liu, W.; Zhang, H. *Energy Environ. Sci.* **2013**, *6*, 3235−3240.
(21) Zhu, G.; Chen, J.; Zhang, T.; Jing, Q.; Wang, Z. L. *Nat. Commun.* **2014**, *5*, 3426 DOI: ; 10.1038/ncomms4426.
(22) Zhang, C.; Tang, W.; Han, C.; Fan, F.; Wang, Z. L. *Adv. Mater.* **2014**, *26*, 3580−3591.
(23) Fan, F. R.; Lin, L.; Zhu, G.; Wu, W.; Zhang, R.; Wang, Z. L. *Nano Lett.* **2012**, *12*, 3109−3114.
(24) Kim, S.; Gupta, M. K.; Lee, K. Y.; Sohn, A.; Kim, T. Y.; Shin, K.-S.; Kim, D.; Kim, S. K.; Lee, K. H.; Shin, H.-J.; Kim, D.-W.; Kim, S.-W. *Adv. Mater.* **2014**, *26*, 3918−3925.
(25) Wang, S.; Lin, L.; Wang, Z. L. *Nano Lett.* **2012**, *12*, 6339−6346.
(26) Lin, Z.-H.; Cheng, G.; Lin, L.; Lee, S.; Wang, Z. L. *Angew. Chem., Int. Ed.* **2013**, *52*, 12545−12549.
(27) Kwon, S.-H.; Park, J.; Kim, W. K.; Yang, Y.; Lee, E.; Han, C. J.; Park, S. Y.; Lee, J.; Kim, Y. S. *Energy Environ. Sci.* **2014**, *7*, 3279−3283.
(28) Lin, L.; Wang, S.; Xie, Y.; Jing, Q.; Niu, S.; Hu, Y.; Wang, Z. L. *Nano Lett.* **2013**, *13*, 2916−2923.
(29) Bai, P.; Zhu, G.; Liu, Y.; Chen, J.; Jing, Q.; Yang, W.; Ma, J.; Zhang, G.; Wang, Z. L. *ACS Nano* **2013**, *7*, 6361−6366.
(30) Yang, Y.; Zhang, H.; Liu, R.; Wen, X.; Hou, T.-C.; Wang, Z. L. *Adv. Energy Mater.* **2013**, *3*, 1563−1568.
(31) Yang, J.; Chen, J.; Yang, Y.; Zhang, H.; Yang, W.; Bai, P.; Su, Y.; Wang, Z. L. *Adv. Energy Mater.* **2014**, *4*, 1301322.
(32) Taghavi, M.; Mattoli, V.; Sadeghi, A.; Mazzolai, B.; Beccai, L. *Adv. Energy Mater.* **2014**, *4*, 1400024.
(33) Lin, Z.-H.; Zhu, G.; Zhou, Y. S.; Yang, Y.; Bai, P.; Chen, J.; Wang, Z. L. *Angew. Chem., Int. Ed.* **2013**, *52*, 5065−5069.
(34) Zhu, G.; Pan, C.; Guo, W.; Chen, C. Y.; Zhou, Y.; Yu, R.; Wang, Z. L. *Nano Lett.* **2012**, *12*, 4960−4965.
(35) Lin, Z.-H.; Xie, Y.; Yang, Y.; Wang, S.; Zhu, G.; Wang, Z. L. *ACS Nano* **2013**, *7*, 4554−4560.
(36) Lin, L.; Xie, Y.; Wang, S.; Wu, W.; Niu, S.; Wen, X.; Wang, Z. L. *ACS Nano* **2013**, *7*, 8266−8274.
(37) Lin, Z.-H.; Cheng, G.; Yang, Y.; Zhou, Y. S.; Lee, S.; Wang, Z. L. *Adv. Funct. Mater.* **2014**, *24*, 2810−2816.
(38) Cheng, G.; Lin, Z.-H.; Du, Z.; Wang, Z. L. *Adv. Funct. Mater.* **2014**, *24*, 2892−2898.
(39) Zheng, Y.; Cheng, L.; Yuan, M.; Wang, Z.; Zhang, L.; Qin, Y.; Jing, T. *Nanoscale* **2014**, *6*, 7842−7846.
(40) Jung, Y. S.; Ross, C. A. *Adv. Mater.* **2009**, *21*, 2540−2545.
(41) Bita, I.; Yang, J. K. W.; Jung, Y. S.; Ross, C. A.; Thomas, E. L.; Berggren, K. K. *Science* **2008**, *321*, 939−943.
(42) Kim, S. O.; Solak, H. H.; Stoykovich, M. P.; Ferrier, N. J.; De Pablo, J. J.; Nealey, P. F. *Nature* **2003**, *424*, 411−414.
(43) Yang, J. K. W.; Jung, Y. S.; Chang, J.-B.; Mickiewicz, R. A.; Alexander-Katz, A.; Ross, C. A.; Berggren, K. K. *Nat. Nanotechnol.* **2010**, *5*, 256−260.
(44) Ross, C. A.; Berggren, K. K.; Cheng, J. Y.; Jung, Y. S.; Chang, J. B. *Adv. Mater.* **2014**, *25*, 4386−4396.
(45) Bang, J.; Jeong, U.; Ryu, D. Y.; Russell, T. P.; J Hawker, C. *Adv. Mater.* **2009**, *21*, 4769−4792.
(46) Jeong, J. W.; Park, W. I.; Kim, M.; Ross, C. A.; Jung, Y. S. *Nano Lett.* **2011**, *11*, 4095−4101.
(47) Jeong, J. W.; Park, W. I.; Do, L. M.; Park, J. H.; Kim, T. H.; Chae, G.; Jung, Y. S. *Adv. Mater.* **2012**, *24*, 3526−3531.
(48) Jeong, J. W.; Hur, Y. H.; Kim, H. J.; Kim, J. M.; Park, W. I.; Kim, M. J.; Kim, B. J.; Jung, Y. S. *ACS Nano* **2013**, *7*, 6747−6757.
(49) Moon, H.-S.; Y, K. J.; Jin, H. M.; Lee, W. J.; Choi, H. J.; Mun, J. H.; Choi, Y. J.; Cha, S. K.; Kwon, S. H.; Kim, S. O. *Adv. Funct. Mater.* **2014**, *24*, 4343−4348.
(50) Kennemur, J. G.; Yao, L.; Bates, F. S.; Hillmyer, M. A. *Macromolecules* **2014**, *47*, 1411−1418.
(51) Park, W. I.; Kim, K.; Jang, H. I.; Jeong, J. W.; Kim, J. M.; Choi, J.; Park, J. H.; Jung, Y. S. *Small* **2012**, *8*, 3762−3768.
(52) Jung, Y. S.; Jung, W.; Tuller, H. L.; Ross, C. A. *Nano Lett.* **2008**, *8*, 3777−3780.
(53) Jeong, C. K.; Jin, H. M.; Ahn, J. H.; Park, T. J.; Yoo, H. G.; Koo, M.; Choi, Y. K.; Kim, S. O.; Lee, K. J. *Small* **2014**, *10*, 337−343.
(54) Park, W. I.; You, B. K.; Mun, B. H.; Seo, H. K.; Lee, J. Y.; Hosaka, S.; Yin, Y.; Ross, C. A.; Lee, K. J.; Jung, Y. S. *ACS Nano* **2013**, *7*, 2651−2658.
(55) Shin, D. O.; Mun, J. H.; Hwang, G. T.; Yoon, J. M.; Kim, J. Y.; Yun, J. M.; Yang, Y. B.; Oh, Y.; Lee, J. Y.; Shin, J.; Lee, K. J.; Park, S.; Kim, J. U.; Kim, S. O. *ACS Nano* **2013**, *7*, 8899−8907.
(56) Park, W. I.; Yoon, J. M.; Park, M.; Lee, J.; Kim, S. K.; Jeong, J. W.; Kim, K.; Jeong, H. Y.; Jeon, S.; No, K. S.; Lee, J. Y.; Jung, Y. S. *Nano Lett.* **2012**, *12*, 1235−1240.
(57) Black, C. T. *Appl. Phys. Lett.* **2005**, *87*, 163116.
(58) Orilall, M. C.; Wiesner, U. *Chem. Soc. Rev.* **2011**, *40*, 520−535.
(59) Ross, C. A.; Cheng, J. Y. *MRS Bull.* **2008**, *33*, 838−845.
(60) Nunns, A.; Gwyther, J.; Manners, I. *Polymer* **2013**, *54*, 1269−1284.
(61) Zhong, J.; Zhong, Q.; Fan, F.; Zhang, Y.; Wang, S.; Hu, B.; Wang, Z. L.; Zhou, J. *Nano Energy* **2013**, *2*, 491−497.
(62) Kim, B. H.; Lee, D. H.; Kim, J. Y.; Shin, D. O.; Jeong, H. Y.; Hong, S.; Yun, J. M.; Koo, C. M.; Lee, H.; Kim, S. O. *Adv. Mater.* **2011**, *23*, 5618−5622.
(63) Niu, S.; Wang, S.; Lin, L.; Liu, Y.; Zhou, Y. S.; Hu, Y.; Wang, Z. L. *Energy Environ. Sci.* **2013**, *6*, 3576−3583.
(64) Yang, W.; Chen, J.; Zhu, G.; Yang, J.; Bai, P.; Su, Y.; Jing, Q.; Cao, X.; Wang, Z. L. *ACS Nano* **2013**, *7*, 11317−11324.
(65) O'Halloran, A.; O'Malley, F.; McHugh, P. *J. Appl. Phys.* **2008**, *104*, 017101.
(66) Watanabe, H.; Hosoi, T. In *Physics and Technology of Silicon Carbide Devices*; Hijikata, Y., Ed.; InTech: Rijeka, Croatia, 2012; pp 235−250.
(67) Burgo, T. A. L.; Ducati, T. R. D.; Francisco, K. R.; Clinckspoor, K. J.; Galembeck, F.; Galembeck, S. E. *Langmuir* **2012**, *28*, 7407−7416.
(68) Burgo, T. A. L.; Silva, C. A.; Balestrin, L. B. S.; Galembeck, F. *Sci. Rep.* **2013**, *3*, 2384.
(69) Balestrin, L. B. S.; Duque, D. D.; Silva, D. S.; Galembeck, F. *Faraday Discuss.* **2014**, DOI: 10.1039/c3fd00118k.
(70) Saurenbach, F.; Wollmann, D.; Terris, B. D.; Diaz, A. F. *Langmuir* **1992**, *8*, 1199−1203.
(71) Lee, S.; Lee, Y.; Kim, D.; Yang, Y.; Lin, L.; Lin, Z. H.; Hwang, W.; Wang, Z. L. *Nano Energy* **2013**, *2*, 1113−1120.
(72) Egitto, F. D.; Matienzo, L. J. *IBM J. Res. Dev.* **1994**, *38*, 423−439.
(73) Hegemann, D.; Brunner, H.; Oehr, C. *Nucl. Instrum. Methods B* **2003**, *208*, 281−286.
(74) Reddy, S.; Schunk, P. R.; Bonnecaze, R. T. *Phys. Fluids* **2005**, *17*, 1−6.
(75) Ko, S. H.; Park, I.; Pan, H.; Grigoropoulos, C. P.; Pisano, A. P.; Luscombe, C. K.; Fréchet, J. M. J. *Nano Lett.* **2007**, *7*, 1869−1877.
(76) Niu, S.; Liu, Y.; Wang, S.; Lin, L.; Zhou, Y. S.; Hu, Y.; Wang, Z. L. *Adv. Funct. Mater.* **2014**, *24*, 3332−3340.
(77) Niu, S.; Liu, Y.; Wang, S.; Lin, L.; Zhou, Y. S.; Hu, Y.; Wang, Z. L. *Adv. Mater.* **2013**, *25*, 6184−6193.
(78) Niu, S.; Wang, S.; Liu, Y.; Zhou, Y. S.; Lin, L.; Hu, Y.; Pradel, K. C.; Wang, Z. L. *Energy Environ. Sci.* **2014**, *7*, 2339−2349.